

SuperNeRF-GAN: A Universal 3D-Consistent Super-Resolution Framework for Efficient and Enhanced 3D-Aware Image Synthesis

Peng Zheng, Linzhi Huang, Yizhou Yu, Yi Chang, Yilin Wang, and Rui Ma

Abstract—Neural volume rendering techniques, such as NeRF, have revolutionized 3D-aware image synthesis by enabling the generation of images of a single scene or object from various camera poses. However, the high computational cost of NeRF presents challenges for synthesizing high-resolution (HR) images. Most existing methods address this issue by leveraging 2D super-resolution, which compromise 3D-consistency. Other methods propose radiance manifolds or two-stage generation to achieve 3D-consistent HR synthesis, yet they are limited to specific synthesis tasks, reducing their universality. To tackle these challenges, we propose SuperNeRF-GAN, a universal framework for 3D-consistent super-resolution. A key highlight of SuperNeRF-GAN is its seamless integration with NeRF-based 3D-aware image synthesis methods and it can simultaneously enhance the resolution of generated images while preserving 3D-consistency and reducing computational cost. Specifically, given a pre-trained generator capable of producing a NeRF representation such as tri-plane, we first perform volume rendering to obtain a low-resolution image with corresponding depth and normal map. Then, we employ a NeRF Super-Resolution module which learns a network to obtain a high-resolution NeRF. Next, we propose a novel Depth-Guided Rendering process which contains three simple yet effective steps, including the construction of a boundary-correct multi-depth map through depth aggregation, a normal-guided depth super-resolution and a depth-guided NeRF rendering. Experimental results demonstrate the superior efficiency, 3D-consistency, and quality of our approach. Additionally, ablation studies confirm the effectiveness of our proposed components.

Index Terms—Generative models, image synthesis, 3D-consistency, super-resolution

I. INTRODUCTION

THE introduction of Neural volume rendering technique, such as NeRF [1]–[4] has significantly advanced 3D-aware image synthesis, enabling the generation of images from various camera poses for a single scene or object. These models learn NeRF representations, which can then be rendered into images at specified camera poses. However, the high computational cost inherent in NeRF limits their ability to synthesize high-resolution (HR) images. To address this, most existing methods [5]–[9] use a 2D super-resolution (SR) module, but this approach often compromises 3D-consistency. While these inconsistencies might not be evident in static images, they become apparent in free-view videos, hindering applications in areas like video games and virtual reality.

Few studies focus on 3D-consistent image synthesis. GRAM-HD [10] proposes using HR radiance manifolds to achieve 3D-consistent HR image synthesis. However, the

TABLE I: Comparison of 3D-aware image synthesis methods based on various criteria.

Method	3D-Consistent	High Efficiency	High-Resolution	High Universality	Image Quality	Geometry Quality
StyleNeRF	✗	✓	✓	✓	✗	✗
StyleSDF	✗	✓	✓	✓	✗	✗
GRAM-HD	✓	✓	✓	✓	✗	✗
EG3D	✗	✓	✗	✓	✓	✓
SH-HD	✓	✗	✓	✗	✓	✓
Ours	✓	✓	✓	✓	✓	✓

inability of GRAM-HD to synthesize images from large viewpoints limits its capability for full-body and full-head image synthesis. SemanticHuman-HD (SH-HD) [11] introduces a two-stage generation strategy for 3D-consistent HR image synthesis. However, it suffers from boundary depth issues due to its simplistic neighbor-aware depth aggregation, leading to failure in portrait synthesis. Other 3D-consistent methods struggles at HR image synthesis due to their high computational cost.

To address these limitations, we propose SuperNeRF-GAN, a universal 3D-consistent super-resolution framework that achieves HR image synthesis while maintaining 3D-consistency. This framework can be seamlessly integrated with NeRF-based 3D-aware image synthesis methods. Given a NeRF representation generated by a pre-trained model, we first perform volume rendering to obtain a low-resolution image with corresponding depth and normal maps. We then employ the NeRF Super-Resolution module, which learns a network to generate a HR NeRF representation. Following this, we introduce a novel Depth-Guided Rendering process that includes constructing a boundary-correct multi-depth map through depth aggregation and normal-guided depth super-resolution, and finally performing depth-guided NeRF rendering to synthesize HR image in a 3D-consistent way.

To evaluate the effectiveness of our method, we apply SuperNeRF-GAN to pre-trained models from state-of-the-art (SOTA) methods for portrait, cat face, and full-body image synthesis. The experimental results demonstrate significant improvements in 3D-consistency and efficiency compared to the original pre-trained models, as well as enhanced universality, 3D-consistency, and quality over other SOTA methods. Additionally, we conduct comparative experiments against other SOTA methods to further validate the superiority of our proposed approach.

This paper was produced by the IEEE Publication Technology Group. They are in Piscataway, NJ.

Manuscript received xxx, 2025; revised xxx, 2025.

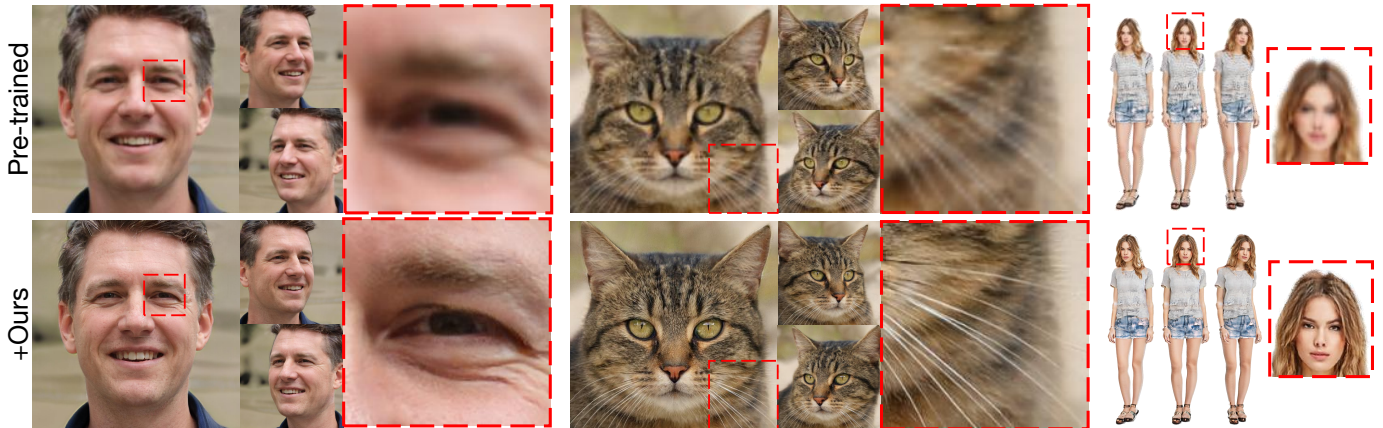


Fig. 1: Effectiveness of our proposed SuperNeRF-GAN. The images in the first row are synthesized by existing pre-trained models, without the use of 2D image super-resolution. The second row shows the images super-resolved by SuperNeRF-GAN in a 3D-consistent way. Please zoom in to see the detailed differences between the original and super-resolved images.

In summary, the main contributions of this paper are:

- We propose SuperNeRF-GAN, a universal 3D-consistent super-resolution framework that enhances the resolution and 3D-consistency of synthesized images. SuperNeRF-GAN is designed to be universally applicable, making it easily deployable on NeRF-based 3D-aware image synthesis methods.
- SuperNeRF-GAN overcomes the limitations of SH-HD and GRAM-HD, which are restricted to specific synthesis tasks. In contrast, SuperNeRF-GAN demonstrates high versatility, making it suitable for various synthesis tasks.
- Quantitative and qualitative results validate the superiority of our proposed method, particularly in terms of 3D-consistency and efficiency.

II. RELATED WORK

A. 3D-Aware Image Synthesis

With the advent of generative adversarial networks (GANs) [12]–[15] and diffusion models [16]–[19], generative models have demonstrated impressive performance in image synthesis. Some works [20]–[22] achieve pose control by integrating parametric models such as SMPL [23] and 3DMM [24]. However, due to the lack of inherent 3D representations, these approaches do not achieve true 3D-aware image synthesis.

GRAF [25] first introduces NeRF [1] into generative models by learning a neural radiance field that can be rendered into an image at a given camera pose. However, using an MLP to model this field results in high computational cost, limiting the ability to synthesize high-quality images. Subsequent works like StyleSDF [26] and StyleNeRF [27] use volume rendering to obtain a low-resolution (LR) image and then upsample it to a high-resolution (HR) image. VolumeGAN [28] employs an explicit 3D feature volume to model the radiance fields, achieving high-fidelity image synthesis. However, increasing the resolution with this 3D volume representation results in a cubic growth in computational cost, making it inefficient for HR synthesis. EG3D [29] addresses this by proposing

a tri-plane representation, reducing the cubic growth to a quadratic level. EG3D achieves SOTA performance in both image and geometry quality, and most current 3D-aware image synthesis methods [30]–[36] build upon it. However, these methods commonly employ a 2D super-resolution module, which compromises 3d-consistency although achieves HR image synthesis. As a result, these methods struggle to maintain 3d-consistency across different camera poses, limiting their application in areas such as virtual reality and video games, where both efficiency and 3d-consistency are crucial.

B. 3D-Consistent HR Image Synthesis

GRAM-HD [10] generates HR radiance manifolds [37] instead of NeRF, thus avoiding the need for dense sampling and direct generation of 3D features. This approach ensures 3d-consistency by eliminating the need for image super-resolution. However, using radiance manifolds leads to suboptimal image and geometry quality. Rather than introducing a new representation like tri-plane or radiance manifolds, SemanticHuman-HD (SH-HD) [11] proposes a two-stage generation strategy that achieves efficient 3D-consistent synthesis without compromising image quality. In the first stage, an LR image with a corresponding depth map is rendered using dense sampling. In the second stage, the depth map is aggregated using neighboring points to produce a multi-channel depth map, which can be unprojected into 3D points instead of relying on dense sampling. Although this method achieves HR image synthesis with 3d-consistency and efficiency, it suffers from boundary depth issues due to its simplistic depth aggregation. This limitation restricts SH-HD to generating depth-smooth images, such as full-body images, and prevents it from generating images in scenarios with more complex depth variations, such as portraits. As for other 3D-consistent methods [38]–[40], they face challenges in HR image synthesis due to their high computational cost.

In conclusion, existing methods struggle to efficiently achieve 3D-consistent HR image synthesis for both portraits and full-body images. Our proposed SuperNeRF-GAN frame-

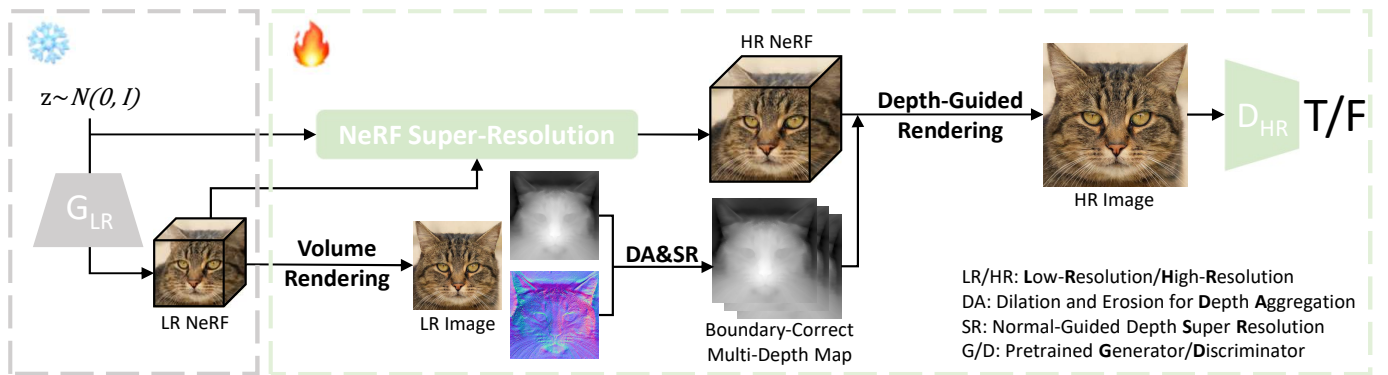


Fig. 2: Pipeline of the proposed SuperNeRF-GAN framework. Given a random noise z , the pre-trained generator of existing 3D generative models maps it to a low-resolution (LR) NeRF representation. This LR representation can be rendered into a corresponding LR image along with depth and normal maps. Next, the LR NeRF representation undergoes the NeRF Super-Resolution module to produce a high-resolution (HR) NeRF representation. Simultaneously, Dilation and Erosion for Depth Aggregation and Normal-Guided Depth Super-Resolution are applied to the LR depth map to construct a boundary-correct multi-depth map. This map guides the rendering process of the HR NeRF representation, enabling efficient and 3D-consistent HR image synthesis.

work addresses these challenges by offering a universal solution that enhances both image and geometry quality while maintaining 3d-consistency across varying viewpoints.

III. METHOD

Figure 2 illustrates the pipeline of our SuperNeRF-GAN framework, which is designed to seamlessly integrate with existing NeRF-based 3D-aware image synthesis methods. For demonstration, we use EG3D [29], a SOTA method in 3D-aware image synthesis, as a case study to introduce our SuperNeRF-GAN pipeline. Initially, our framework leverages the tri-plane representation produced by the pre-trained EG3D model to render a low-resolution image, along with associated depth and normal maps. Unlike EG3D, which performs image super-resolution in a 2D manner, our approach maintains 3D-consistency throughout the process. Specifically, we employ the NeRF Super-Resolution module and the Boundary-Correct Multi-Depth Construction technique to generate the high-resolution (HR) tri-plane representation and depth map. These components are then utilized in the Depth-Guided Rendering process, which efficiently synthesizes HR images while preserving 3D-consistency. To fully understand our methodology, we first introduce the essential preliminaries, including volume rendering [1] and EG3D [29].

A. Preliminary

1) *Volume Rendering*: NeRF [1] introduces volume rendering to synthesize images from given camera poses. For each pixel, a ray $\mathbf{r}(t)$ is cast from the camera position \mathbf{o} along the direction \mathbf{d} : $\mathbf{r}(t) = \mathbf{o} + t\mathbf{d}$, where t represents the distance from the camera position. The color $C(\mathbf{r})$ of this pixel is accumulated along the ray using volume rendering, which can be formulated as:

$$C(\mathbf{r}) = \int_{t_n}^{t_f} T(t) \cdot \sigma(\mathbf{r}(t)) \cdot \mathbf{c}(\mathbf{r}(t)) \cdot dt, \quad (1)$$

$$\text{where } T(t) = \exp\left(-\int_{t_n}^t \sigma(\mathbf{r}(s)) ds\right). \quad (2)$$

Here, $\mathbf{c}(\mathbf{r}(t))$ and $\sigma(\mathbf{r}(t))$ denote the color and density of the 3D point $\mathbf{r}(t)$, respectively, while $T(t)$ represents the accumulated transmittance along the ray from t_n to t . Notably, by replacing the color $\mathbf{c}(\mathbf{r}(t))$ with the normal value $\mathbf{n}(\mathbf{r}(t))$ and distance t , this formula can also be used to render the normal value $N(\mathbf{r})$ and depth value $D(\mathbf{r})$ of the ray. In practice, this formula is discretized. For more details about volume rendering, please refer to NeRF.

2) *EG3D as Pre-trained 3D Generator*: The generator of EG3D is adapted from StyleGAN2 [14], which achieves SOTA performance in image synthesis. Given a random noise \mathbf{z} sampled from a Gaussian distribution, the generator maps it into a feature map with dimensions $256 \times 256 \times 96$. This feature map is then reshaped into a tri-plane representation \mathbf{T}_{LR} , where the three planes correspond to the XY, YZ, and ZX orientations. Each plane consists of 32 channels with a resolution of 256×256 . For a 3D point \mathbf{X} , we project it onto these three planes and perform bilinear interpolation to extract its features from each plane. These features are then fed into an MLP, which outputs the color $\mathbf{c}(\mathbf{X})$ and density $\sigma(\mathbf{X})$. These values are subsequently used in volume rendering, as described in Eq 1.

B. 3D-Consistent Low-Resolution Image Synthesis

Using random noise \mathbf{z} as input, the pre-trained EG3D model generates a low-resolution tri-plane representation \mathbf{T}_{LR} . This representation is rendered from a given camera pose to produce a low-resolution image \mathbf{I}_{LR} , along with the corresponding depth map \mathbf{D}_{LR} and normal map \mathbf{N}_{LR} , each at a resolution of 256^2 . In this process of low-resolution image synthesis, we employ dense sampling as used in EG3D. Specifically, for each pixel, 36 points are sampled along the ray using uniform sampling and an additional 36 points using importance sampling. Although dense sampling is computationally intensive,

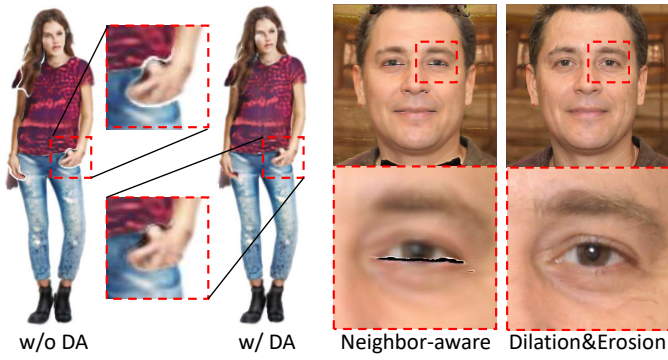


Fig. 3: The left two figures demonstrate the effectiveness of Depth Aggregation (DA), note that the results are synthesized by untrained SuperNeRF-GAN models for better demonstration. The right two compare different DA techniques, highlighting that Neighbor-aware DA in SH-HD introduces noticeable artifacts, especially at depth discontinuities.

its overall computational cost remains manageable due to the low resolution of the output.

C. 3D-Consistent Super-Resolution

1) *NeRF Super-Resolution*: To obtain an HR 3D representation \mathbf{T}_{HR} , we utilize the NeRF Super-Resolution module, which is based on the architecture of StyleGAN2. This module takes the LR tri-plane representation \mathbf{T}_{LR} and the corresponding noise \mathbf{z} as input, and outputs an HR representation \mathbf{T}_{HR} at a resolution of 1024^2 . Importantly, the module uses the same noise \mathbf{z} as the pre-trained 3D generator to ensure consistency in the distribution between LR and HR images.

2) *Depth-Guided Rendering*: We construct an HR multi-depth map \mathbf{D}_{HR} with three channels using the Boundary-Correct Multi-Depth Map Construction, which will be detailed in the next section. This map is used to guide the sampling process, thereby avoiding the dense sampling employed by EG3D. Our Depth-Guided Rendering approach is modified from Eq. 1, and is formulated as follows:

$$C(\mathbf{r}) = \sum_{i=1}^3 T_i (1 - \exp(-\sigma_i \delta_i)) \mathbf{c}_i, \quad (3)$$

$$\text{where } T_i = \exp\left(-\sum_{j=1}^{i-1} \sigma_j \delta_j\right). \quad (4)$$

Here, $\delta_i = \mathbf{D}_{i+1} - \mathbf{D}_i$ represents the distance between adjacent depth values, where \mathbf{D}_i is the i th value of \mathbf{D}_{HR} . σ_i and \mathbf{c}_i are the density and color interpolated from the HR 3D representation, with the interpolation coordinates projected from the depth map. Notably, as shown in Eq. 3, the number of sampling points is reduced from 64 (as explained in "3D-Consistent LR Image Synthesis") to 3, achieving efficient rendering at a 1024^2 resolution.

D. Boundary-Correct Multi-Depth Map Construction

As introduced in the Depth-Guided Rendering section, we need a multi-depth map to guide the rendering. This section

details how to construct this map. A straightforward approach is to perform bilinear interpolation on the low-resolution (LR) depth map \mathbf{D}_{LR} . However, this often leads to incorrect depth values at the boundaries due to depth discontinuities. Specifically, consider two adjacent pixels on the boundary, which have non-continuous depth values. Direct interpolation will result in an averaged value that does not align with either of the two pixels' actual depth values.

To address the boundary depth issue, SH-HD [11] proposes aggregating depth values of neighboring pixels before performing bilinear interpolation on the depth map. While this method is effective for full-body image synthesis, it struggles with portrait synthesis. This limitation arises because neighbor-aware depth aggregation does not fundamentally solve the boundary issue but merely alleviates it. Therefore, SH-HD performs well in depth-smooth scenarios, such as full-body image synthesis, but fails in other cases. To obtain a boundary-correct high-resolution depth map, our solution involves Dilation and Erosion for Depth Aggregation and Normal-Guided Depth Super-Resolution, which are introduced below.

1) *Dilation and Erosion for Depth Aggregation*: Different from SH-HD, we employ erosion and dilation operations to aggregate the depth map. Erosion is a morphological operation that shrinks the boundaries of objects in an image. For a given depth map \mathbf{D} and a structuring element B , the erosion operation is formulated as:

$$(\mathbf{D} \ominus B)(x, y) = \min_{(s,t) \in B} \{\mathbf{D}(x+s, y+t) - B(s, t)\}, \quad (5)$$

where (x, y) are the coordinates of a pixel in the depth map \mathbf{D} , and (s, t) are the coordinates within the structuring element B . This operation slides the structuring element B over the image \mathbf{D} and replaces each pixel by the minimum value of the image pixels covered by B minus the corresponding value of B . Conversely, dilation expands the boundaries of objects in an image. The dilation operation is formulated as:

$$(\mathbf{D} \oplus B)(x, y) = \max_{(s,t) \in B} \{\mathbf{D}(x+s, y+t) + B(s, t)\}. \quad (6)$$

The choice of the structuring element B significantly affects the results of erosion and dilation. In our case, we use a square structuring element. By applying erosion and dilation to the LR depth map \mathbf{D}_{LR} , we obtain the dilated depth map \mathbf{D}_{dil} and eroded depth map \mathbf{D}_{ero} , which are then concatenated with \mathbf{D}_{LR} , resulting in an aggregated map \mathbf{D}_{agg} with three channels. This aggregated map addresses the boundary depth issue by storing depth values from both sides of the boundary, as shown in Figure 3 (right).

2) *Normal-Guided Depth Super-Resolution*: Naive bilinear interpolation on the aggregated depth map results in multi depth values at boundaries, which include values from both sides of the boundary. However, these depth values may not be accurate as the bilinear interpolation relies solely on the information within the aggregated depth map. To address this, we propose a Normal-Guided Depth Super-Resolution module, which leverages the normal map to provide supplementary geometric information.

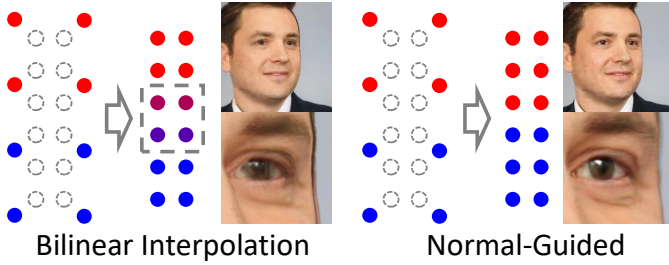


Fig. 4: Effectiveness of Normal-Guided Depth Super-Resolution. The dashed rectangle highlights inaccuracies at depth discontinuity using bilinear interpolation, which result in artifacts as in the synthesized image.

Given a normal map $\mathbf{N} = (N_x, N_y, N_z)$, the differences in depth values can be computed as: $\Delta_x = N_x/N_z$ and $\Delta_y = N_y/N_z$. The super-resolved depth map \mathbf{D}_{SR} at 512^2 resolution can be expressed as the original depth map plus the differences with respect to x and y , formulated as:

$$\mathbf{D}_{SR}(x, y) = \mathbf{D}_{LR}(m, n) + \Delta(x, y), \quad (7)$$

$$\Delta(x, y) = \frac{w_x(x, y) \cdot \Delta_x(m, n) + w_y(x, y) \cdot \Delta_y(m, n)}{\sqrt{(\Delta_x(m, n))^2 + (\Delta_y(m, n))^2}}, \quad (8)$$

where $w_x(x, y)$ and $w_y(x, y)$ are weight functions dependent on x and y . The weight function is defined as:

$$w_x(x, y) = \frac{e^{-|\Delta_x(m, n)|}}{e^{-|\Delta_x(m, n)|} + e^{-|\Delta_y(m, n)|}} \cdot (-1)^{\mathbb{I}(x=2m-1)}, \quad (9)$$

where \mathbb{I} is an indicator function while m and n are integers related to the coordinates x and y by:

$$m = \left\lfloor \frac{x+1}{2} \right\rfloor, \quad n = \left\lfloor \frac{y+1}{2} \right\rfloor. \quad (10)$$

The remaining part of the weight function is a softmax function inspired by BiNi [41], which assumes that the depth map is semi-smooth. This means that the depth map is one-sided differentiable, with larger weight assigned to the direction with smaller differences.

Consequently, the aggregated depth map \mathbf{D}_{agg} is processed through the Normal-Guided Depth Super-Resolution module twice, resulting in a boundary-correct multi-depth map \mathbf{D}_{HR} at 1024^2 resolution. Notably, to facilitate Depth-Guided Rendering, the three-channel depth values of this multi-depth map are sorted. A visualization of this module is provided in Figure 4.

E. Training Pipeline

1) *Training Strategy*: Our method can be directly applied to pre-trained 3D generative models, such as EG3D and SH-HD. During training, we freeze the pre-trained generator and focus on training the NeRF Super-Resolution module. Notably, the discriminator has been redesigned to process high-resolution images and is tunable during training.

2) *Loss Function*: We use the loss functions from the original method to ensure training consistency. Additionally, we adopt the unsample loss from SH-HD to guide the training of the NeRF Super-Resolution module by penalizing inconsistency between high-resolution and low-resolution images.

TABLE II: Effectiveness our proposed SuperNeRF-GAN. Note that all KID scores in this paper are multiplied by 1000.

Dataset	Method	FID↓	KID↓	PSNR↑	SSIM↑	Res
FFHQ	EG3D	4.65	1.27	33.67	0.893	512
	+SuperNeRF-GAN	5.13	1.70	34.36	0.920	512
		5.10	1.54	36.44	0.935	1024
AFHQ	EG3D	3.19	0.38	32.61	0.843	512
	+SuperNeRF-GAN	3.77	1.09	33.01	0.861	512

TABLE III: Quantitative comparison with SH-HD. "Mem" indicates the GPU memory consumption during training. Since SH-HD is not directly applicable to the FFHQ and AFHQ datasets, we modified it to enable training on these datasets.

Method	DeepFashion1024			FFHQ1024			AFHQ512		
	FID↓	KID↓	Mem	FID↓	KID↓	Mem	FID↓	KID↓	Mem
SH-HD	8.70	4.04	31G	31.9	27.8	25G	8.77	11.7	12G
Ours	8.47	3.68	14G	5.10	1.54	11G	3.77	1.09	8G

IV. IMPLEMENTATION DETAILS

1) *Training Setup*: Our experiments were conducted on a server equipped with 4 NVIDIA A40 GPUs, each with 48GB of memory. The models are trained over a period of 2 to 4 days, depending on the complexity and size of the dataset. Specifically, for portrait and cat face image synthesis tasks, we used a batch size of 16, while a batch size of 4 was employed for full-body image synthesis due to the increased computational demands.

2) *SH-HD for Portrait and Cat Face Image Synthesis*: To facilitate portrait and cat face image synthesis, we integrate key components from SH-HD [11] into pre-trained EG3D models. These components include the two-stage generation strategy, feature super-resolution module, unsample loss, and neighborhood-aware depth aggregation technique. Despite these adaptations, SH-HD exhibits limitations in portrait and cat face image synthesis, resulting in a drop in image quality for these specific tasks, as demonstrated in Fig. 3. The results underscore the superior universality of our proposed method.

V. EXPERIMENTS

1) *Datasets*: We train our models on three distinct datasets for specific synthesis tasks: FFHQ [13], which includes 50K portrait images at a resolution of 1024^2 , is used for portrait synthesis. For cat face synthesis, we use the AFHQ [42], which contains 5.5K cat face images at a resolution of 1024^2 . For full-body image synthesis, we employ DeepFashion [43], which provides 7K full-body images at a resolution of 1024^2 , along with corresponding segmentation maps. Additionally, due to the requirement in SH-HD [11], we also incorporate normal maps from SH-HD and human poses from AG3D [30].

2) *Baselines*: For portrait and cat face image synthesis, our model leverages pre-trained EG3D [29] models. We compare our results with GRAM-HD [10], StyleNeRF [27], and StyleSDF [26], all recognized for their high-resolution image synthesis capabilities. For full-body image synthesis, our

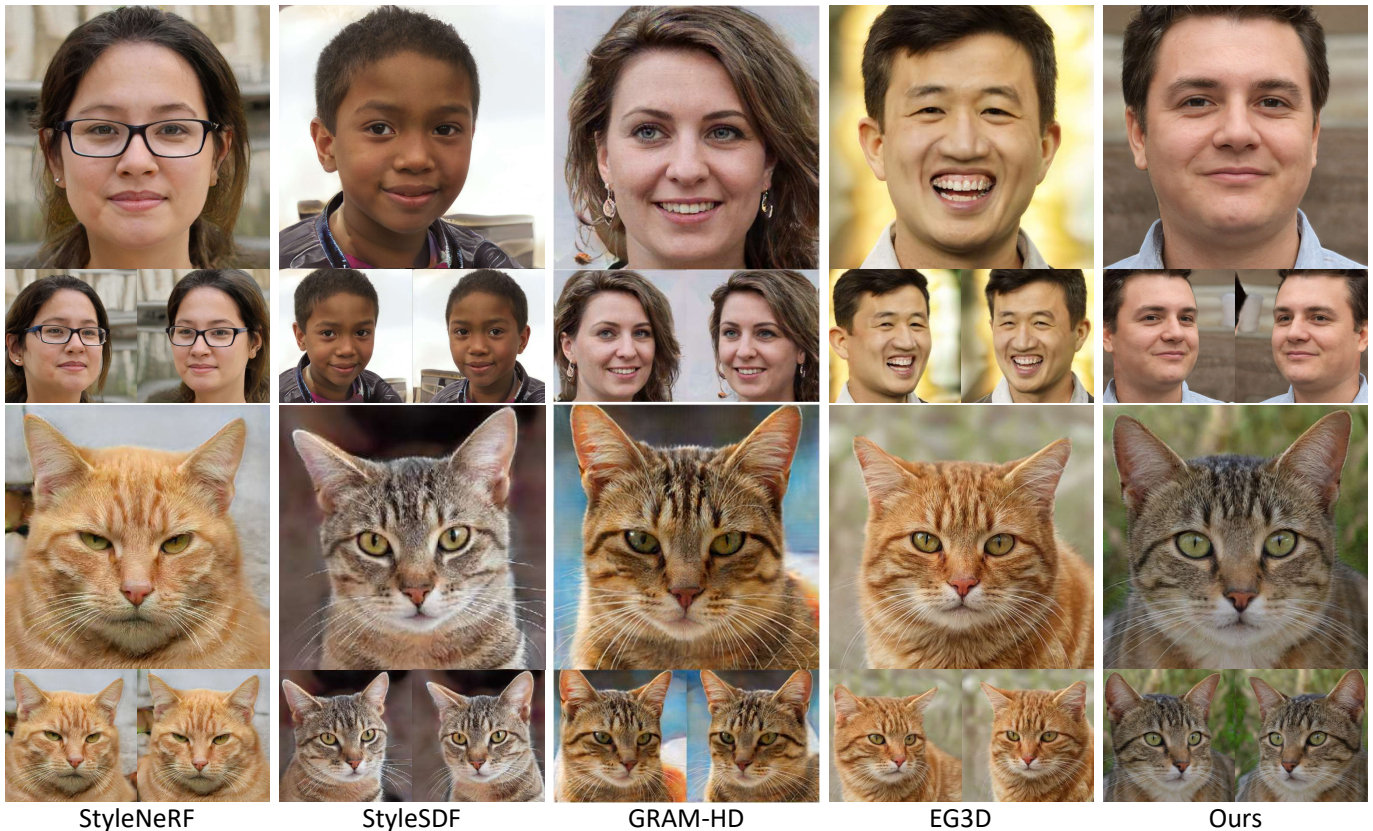


Fig. 5: Qualitative comparison among 3D-aware image synthesis methods. The results of other methods are taken from their respective papers to ensure a fair and consistent comparison. Since the 3D-inconsistency might not be evident in static images, we provide additional comparisons of 3D-consistency in our **Supplementary Video**, where StyleNeRF, StyleSDF, and EG3D show noticeable inconsistencies.

TABLE IV: Quantitative comparison of 3D-consistency. *Results taken from GRAM-HD.

Method	FFHQ1024		AFHQ512	
	PSNR \uparrow	SSIM \uparrow	PSNR \uparrow	SSIM \uparrow
StyleNeRF*	30.0	0.804	-	-
StyleSDF*	31.1	0.836	26.6	0.749
GRAM-HD*	33.8	0.872	28.8	0.807
Ours	36.4	0.935	33.0	0.861

model builds on the pre-trained SH-HD model. We compare it with EVA3D, Veri3D, and GSM, which are noted for their 3D-consistent image synthesis.

3) *Evaluation Metrics*: We use Frchet Inception Distance (FID) [44] and Kernel Inception Distance (KID) [45] to assess the quality of synthesized images. Note that all KID scores are multiplied by 1000. To evaluate 3D-consistency across images synthesized from different camera poses, we adopt Peak Signal-to-Noise Ratio (PSNR) and Structural Similarity (SSIM) metrics, as used in GRAM-HD. Higher scores indicate better 3D-consistency. Specifically, we reconstruct a NeuS [46] model from images synthesized from various camera angles and calculate the PSNR and SSIM scores between the synthesized and reconstructed images. These scores are averaged across 50 entities. For each entity, we generate images from

TABLE V: Quantitative comparison of image quality among methods that achieve high-resolution (1024×1024) image synthesis. *Results are taken from GRAM-HD.

Method	FFHQ1024		AFHQ512	
	FID \downarrow	KID \downarrow	FID \downarrow	KID \downarrow
StyleNeRF*	9.45	2.65	-	-
StyleSDF*	9.44	2.83	7.91	3.90
GRAM-HD*	12.0	5.23	7.67	3.41
Ours	5.10	1.54	3.77	1.09

30 uniformly sampled yaw angles ranging from -0.4 to 0.4 radians. These images are subsequently used to construct a NeuS [46] representation, utilizing NeuS’s default settings to ensure consistency and comparability in our experiments. The constructed NeuS representation is subsequently rendered into reconstructed images from the specified angles to facilitate evaluation.

A. Comparisons

We evaluate 3D-aware image synthesis methods across various criteria, with the results presented in Table I. Note that only our method achieves 3D-consistent HR image synthesis with high universality. Specifically, GRAM-HD is unable to synthesize full-body images due to inherent limitations in its

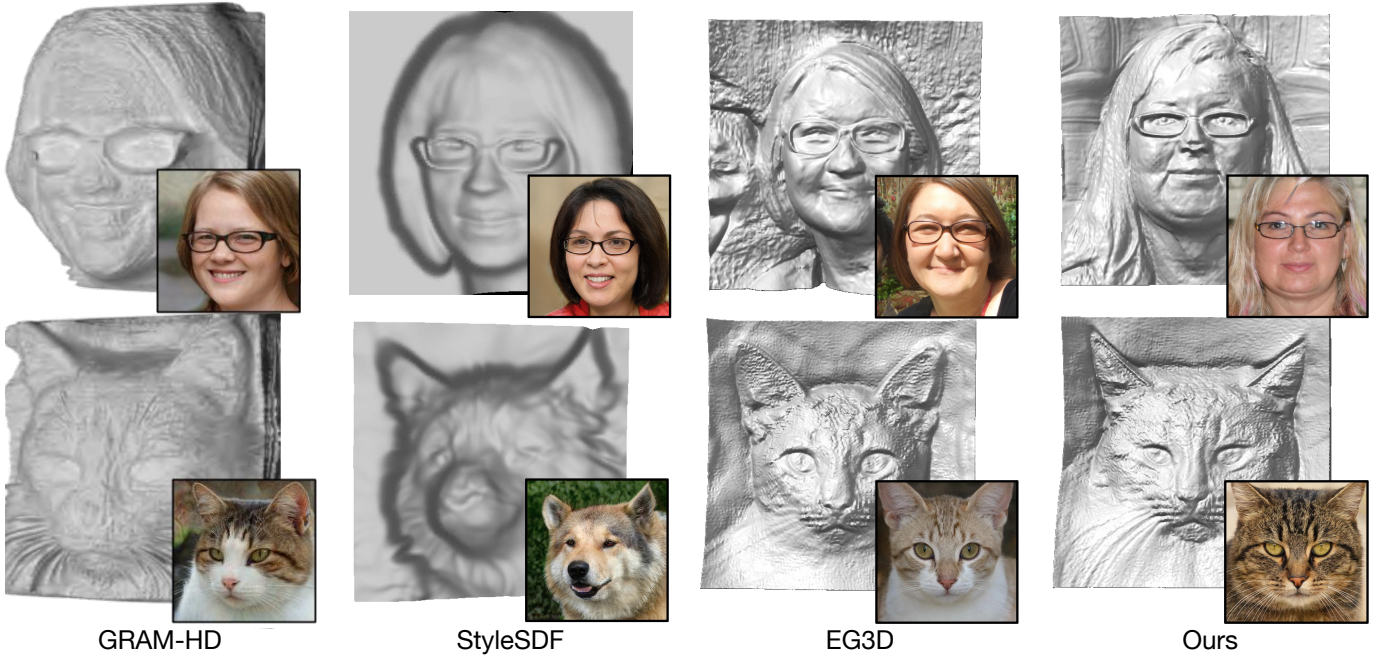


Fig. 6: Qualitative comparison of geometry quality. EG3D and our method generate results with more detailed geometry than other methods.

TABLE VI: Quantitative comparison among methods that achieve full-body image synthesis with 3D-consistency. *Results taken from their papers.

Method	FID↓	KID↓	Resolution	Memory
EVA3D	15.89	9.25	512	33G
GSM	15.78*	-	512	-
VeRi3D	21.4*	-	512	34G
SH-HD	8.70	4.04	1024	31G
Ours	10.56	5.60	512	11G
	8.47	3.68	1024	14G

manifolds, and SH-HD struggles with generating high-quality portraits because of boundary issues, which restrict their universality. As our models are deployed on the pre-trained 3D generators of EG3D and SH-HD, we compare our approach with these methods, as illustrated in Table II and III. Compared to EG3D, our method shows stable improvements in 3D-consistency, albeit with a slight compromise in image quality. We argue that the 2D super resolution used in EG3D significantly improve the image quality, whereas SuperNeRF-GAN leverages Depth-Guided Rendering to ensure 3D-consistency. As for SH-HD, which also ensures 3D-consistency, our method outperforms it in both efficiency and image quality. Notably, SH-HD performances poorly on the FFHQ and AFHQ datasets due to its naive depth aggregation technique. Detailed comparisons with other methods are provided below or in the supplementary materials.

1) *3D-Consistency*: The comparison of 3D-consistency is shown in Table IV. StyleNeRF and StyleSDF exhibit poorer 3D-consistency due to their 2D super-resolution module. While GRAM-HD performs better than the aforementioned methods, its radiance manifolds constrain image quality. Con-

sequently, our method consistently delivers superior performance in both 3D-consistency and image quality. We also present additional qualitative comparison between various 3D-aware image synthesis methods, as illustrated in Fig. 5. The results from other methods were directly taken from their respective publications to ensure a fair and consistent comparison. Since 3D-inconsistency might not be evident in static images, we provide additional comparisons of 3D-consistency in our **Supplementary Video**, where StyleNeRF, StyleSDF, and EG3D show noticeable inconsistencies. In contrast, both GRAM-HD and our method achieve 3D-consistent synthesis. However, GRAM-HD introduces artifacts when viewed from large angles, where our method performs well.

2) *Image Quality*: In terms of image quality, our method shows significant improvements, as shown in Table V. Notably, although GRAM-HD employs generative radiance manifolds to achieve 3D-consistent image synthesis, it compromises on image quality. In contrast, our method achieves superior performance in both image quality and 3D-consistency. Additionally, we evaluated the image quality of 3D-consistent methods on full-body image synthesis task, with results presented in Table VI. Our method not only achieves the highest image quality but also supports high-resolution image synthesis, thanks to our efficient 3D-consistent super-resolution module.

3) *Efficiency*: Our method significantly enhances efficiency in high-resolution image synthesis due to its Depth-Guided Rendering approach, which reduces the number of sampling points. To assess the efficiency of our method, we perform comparative experiments with other 3D-consistent image synthesis methods. As shown in Table VI, our method offers substantial improvements in efficiency, achieving 1024² resolution image synthesis with only 14G of GPU memory.



Fig. 7: Embedding of images at a resolution of 1024^2 using GAN inversion technique.

TABLE VII: Ablation study on depth aggregation methods. "D&E" denotes the dilation and erosion operations used in our method, while $(D\&E)^2$ signifies performing dilation and erosion twice to yield 5 depth values per pixel.

Method	DeepFashion		FFHQ1024		AFHQ512	
	FID↓	KID↓	FID↓	KID↓	FID↓	KID↓
$(D\&E)^2$	9.10	4.71	6.47	2.95	4.50	1.27
D&E	8.47	3.68	5.10	1.54	3.77	1.09

TABLE VIII: Ablation study on interpolation methods. Our proposed Normal-Guided Super-Resolution achieve improvements on 3D-consistency. The results are under 1024^2 resolution to better show the improvements.

Method	FID↓	KID↓	PSNR↑	SSIM↑
Bilinear Interpolation	5.08	1.51	35.75	0.915
Normal-Guided	5.08	1.48	36.44	0.935

4) *Geometry Quality*: We conduct a qualitative comparison of geometry quality, as illustrated in Fig. 6. Due to limitations in radiance manifolds, GRAM-HD struggles to produce high-quality geometry results. StyleSDF generates NeRF representations at a lower resolution, which constrains its ability to produce detailed geometry. In contrast, our method integrates seamlessly with existing NeRF-based approaches, resulting in superior geometry quality.

B. Ablation Study

1) *Depth Aggregation*: The results in Fig. 3 confirm the effectiveness of depth aggregation. We also perform a quantitative ablation study on this technique, presented in Table VII. Specifically, by applying additional dilation and erosion operations, we generate a 5-channel aggregated depth map. The results indicate that doubling the depth aggregation dose not further improve performance, as it introduces depth inaccuracies. Although our Normal-Guided Depth Super-Resolution



Fig. 8: 3D-consistent image synthesis. The images synthesized from different camera poses exhibit consistent 3D structures.

mitigates this issue, the added complexity does not yield additional benefits.

2) *Normal-Guided Depth Super-Resolution*: To assess the effectiveness of our proposed Normal-Guided Depth Super-Resolution module, we conduct a quantitative comparison with bilinear interpolation. The results in Table VIII show that our method achieves notable improvements in 3D-consistency. This improvement is due to our module's ability to accurately super-resolve the depth map with the guidance of the normal map, as demonstrated in Fig. 4.



Fig. 9: High-resolution (1024×1024) portrait synthesis. Our method produces high-quality portraits with rich details.

C. Applications

1) *GAN Inversion*: Our method can be integrated with existing 3D generative models to embed target images into the latent space of our super-resolved model. This embedding is achieved using GAN inversion techniques, which enable the recovery of high-fidelity images at a resolution of 1024^2 , as shown in Fig. 7. Additionally, we explore further applications, such as 3D-consistent image synthesis and style interpolation, which are detailed in the Supplementary Materials.

2) *3D-Consistent Image Synthesis*: In Fig. 8, we showcase images synthesized from different camera poses. The results clearly demonstrate the high level of 3D-consistency achieved by our method. For an even more comprehensive demonstration of 3D-consistent image synthesis, please refer to our **Supplementary Video**, which provide dynamic visualizations that further highlight the 3D-consistency of our approach.

3) *High-Resolution Image Synthesis*: Fig. 9 showcases high-resolution (1024×1024) portrait images synthesized using our method. To balance image quality and diversity, we use a truncation technique where the latent code w is defined as a weighted average of two components: $w = 0.5 \times w_{\text{averaged}} + 0.5 \times w_{\text{random}}$. Here, w_{averaged} is the mean latent code across the dataset, ensuring stable and high-quality synthesis, while w_{random} introduces variability to enhance diversity.

VI. CONCLUSION

In this paper, we present SuperNeRF-GAN, a universal framework for 3D-consistent super-resolution. SuperNeRF-GAN can be seamlessly integrated with existing 3D-aware

image synthesis methods to enhance the resolution of synthesized images while maintaining 3D-consistency and efficiency. The core innovation of SuperNeRF-GAN lies in generating a boundary-correct multi-depth map, which is employed in depth-guided rendering to achieve high-resolution image synthesis with enhanced 3D-consistency and efficiency. Compared to existing 3D-consistent methods, our approach consistently demonstrates improvements in both universality and quality. Meanwhile, it is important to note that while our super-resolution framework ensures 3D-consistency, it slightly compromises image quality compared to methods employing 2D image super-resolution. How to achieve 3D-consistent high resolution image synthesis while ensuring the high image quality similar to the 2D-based methods is still worthy to investigate for realistic image synthesis.

REFERENCES

- [1] B. Mildenhall, P. P. Srinivasan, M. Tancik, J. T. Barron, R. Ramamoorthi, and R. Ng, “Nerf: Representing scenes as neural radiance fields for view synthesis,” *Communications of the ACM*, vol. 65, no. 1, pp. 99–106, 2021.
- [2] J. T. Barron, B. Mildenhall, M. Tancik, P. Hedman, R. Martin-Brualla, and P. P. Srinivasan, “Mip-nerf: A multiscale representation for anti-aliasing neural radiance fields,” in *Proceedings of the IEEE/CVF international conference on computer vision*, 2021, pp. 5855–5864.
- [3] J. T. Barron, B. Mildenhall, D. Verbin, P. P. Srinivasan, and P. Hedman, “Mip-nerf 360: Unbounded anti-aliased neural radiance fields,” in *Proceedings of the IEEE/CVF conference on computer vision and pattern recognition*, 2022, pp. 5470–5479.
- [4] A. Chen, Z. Xu, A. Geiger, J. Yu, and H. Su, “Tensorf: Tensorial radiance fields,” in *European conference on computer vision*. Springer, 2022, pp. 333–350.

- [5] R. Liu, P. Zheng, Y. Wang, and R. Ma, “3d-ssgan: Lifting 2d semantics for 3d-aware compositional portrait synthesis,” *arXiv preprint arXiv:2401.03764*, 2024.
- [6] T. Ma, B. Li, Q. He, J. Dong, and T. Tan, “Semantic 3d-aware portrait synthesis and manipulation based on compositional neural radiance field,” *arXiv preprint arXiv:2302.01579*, 2023.
- [7] F. Yang, T. Chen, X. He, Z. Cai, L. Yang, S. Wu, and G. Lin, “Attrihuman-3d: Editable 3d human avatar generation with attribute decomposition and indexing,” *arXiv preprint arXiv:2312.02209*, 2023.
- [8] K. Deng, G. Yang, D. Ramanan, and J.-Y. Zhu, “3d-aware conditional image synthesis,” in *Proceedings of the IEEE/CVF Conference on Computer Vision and Pattern Recognition*, 2023, pp. 4434–4445.
- [9] T. Wang, B. Zhang, T. Zhang, S. Gu, J. Bao, T. Baltrusaitis, J. Shen, D. Chen, F. Wen, Q. Chen *et al.*, “Rodin: A generative model for sculpting 3d digital avatars using diffusion,” in *Proceedings of the IEEE/CVF conference on computer vision and pattern recognition*, 2023, pp. 4563–4573.
- [10] J. Xiang, J. Yang, Y. Deng, and X. Tong, “Gram-hd: 3d-consistent image generation at high resolution with generative radiance manifolds,” in *Proceedings of the IEEE/CVF International Conference on Computer Vision*, 2023, pp. 2195–2205.
- [11] P. Zheng, T. Liu, Z. Yi, and R. Ma, “Semantichuman-hd: High-resolution semantic disentangled 3d human generation,” *arXiv preprint arXiv:2403.10166*, 2024.
- [12] I. Goodfellow, J. Pouget-Abadie, M. Mirza, B. Xu, D. Warde-Farley, S. Ozair, A. Courville, and Y. Bengio, “Generative adversarial nets,” *Advances in neural information processing systems*, vol. 27, 2014.
- [13] T. Karras, S. Laine, and T. Aila, “A style-based generator architecture for generative adversarial networks,” in *Proceedings of the IEEE/CVF conference on computer vision and pattern recognition*, 2019, pp. 4401–4410.
- [14] T. Karras, S. Laine, M. Aittala, J. Hellsten, J. Lehtinen, and T. Aila, “Analyzing and improving the image quality of stylegan,” in *Proceedings of the IEEE/CVF conference on computer vision and pattern recognition*, 2020, pp. 8110–8119.
- [15] Y. Shi, X. Yang, Y. Wan, and X. Shen, “Semanticstylegan: Learning compositional generative priors for controllable image synthesis and editing,” in *Proceedings of the IEEE/CVF Conference on Computer Vision and Pattern Recognition*, 2022, pp. 11 254–11 264.
- [16] J. Ho, A. Jain, and P. Abbeel, “Denoising diffusion probabilistic models,” *Advances in neural information processing systems*, vol. 33, pp. 6840–6851, 2020.
- [17] T. Brooks, A. Holynski, and A. A. Efros, “Instructpix2pix: Learning to follow image editing instructions,” in *Proceedings of the IEEE/CVF Conference on Computer Vision and Pattern Recognition*, 2023, pp. 18 392–18 402.
- [18] R. Rombach, A. Blattmann, D. Lorenz, P. Esser, and B. Ommer, “High-resolution image synthesis with latent diffusion models,” in *Proceedings of the IEEE/CVF conference on computer vision and pattern recognition*, 2022, pp. 10 684–10 695.
- [19] N. Ruiz, Y. Li, V. Jampani, Y. Pritch, M. Rubinstein, and K. Aberman, “Dreambooth: Fine tuning text-to-image diffusion models for subject-driven generation,” in *Proceedings of the IEEE/CVF conference on computer vision and pattern recognition*, 2023, pp. 22 500–22 510.
- [20] A. Tewari, M. Elgharib, G. Bharaj, F. Bernard, H.-P. Seidel, P. Pérez, M. Zollhofer, and C. Theobalt, “Stylerig: Rigging stylegan for 3d control over portrait images,” in *Proceedings of the IEEE/CVF Conference on Computer Vision and Pattern Recognition*, 2020, pp. 6142–6151.
- [21] K. Sarkar, V. Golyanik, L. Liu, and C. Theobalt, “Style and pose control for image synthesis of humans from a single monocular view,” *arXiv preprint arXiv:2102.11263*, 2021.
- [22] R. Abdal, P. Zhu, N. J. Mitra, and P. Wonka, “Styleflow: Attribute-conditioned exploration of stylegan-generated images using conditional continuous normalizing flows,” *ACM Transactions on Graphics (ToG)*, vol. 40, no. 3, pp. 1–21, 2021.
- [23] F. Bogo, A. Kanazawa, C. Lassner, P. Gehler, J. Romero, and M. J. Black, “Keep it smpl: Automatic estimation of 3d human pose and shape from a single image,” in *Computer Vision—ECCV 2016: 14th European Conference, Amsterdam, The Netherlands, October 11–14, 2016, Proceedings, Part V 14*. Springer, 2016, pp. 561–578.
- [24] B. Egger, W. A. Smith, A. Tewari, S. Wuhler, M. Zollhofer, T. Beeler, F. Bernard, T. Bolkart, A. Kortylewski, S. Romdhani *et al.*, “3d morphable face models—past, present, and future,” *ACM Transactions on Graphics (ToG)*, vol. 39, no. 5, pp. 1–38, 2020.
- [25] K. Schwarz, Y. Liao, M. Niemeyer, and A. Geiger, “Graf: Generative radiance fields for 3d-aware image synthesis,” *Advances in Neural Information Processing Systems*, vol. 33, pp. 20 154–20 166, 2020.
- [26] R. Or-El, X. Luo, M. Shan, E. Shechtman, J. J. Park, and I. Kemelmacher-Shlizerman, “Style sdf: High-resolution 3d-consistent image and geometry generation,” in *Proceedings of the IEEE/CVF Conference on Computer Vision and Pattern Recognition*, 2022, pp. 13 503–13 513.
- [27] J. Gu, L. Liu, P. Wang, and C. Theobalt, “Stylenerf: A style-based 3d-aware generator for high-resolution image synthesis,” *arXiv preprint arXiv:2110.08985*, 2021.
- [28] Y. Xu, S. Peng, C. Yang, Y. Shen, and B. Zhou, “3d-aware image synthesis via learning structural and textural representations,” in *Proceedings of the IEEE/CVF conference on computer vision and pattern recognition*, 2022, pp. 18 430–18 439.
- [29] E. R. Chan, C. Z. Lin, M. A. Chan, K. Nagano, B. Pan, S. De Mello, O. Gallo, L. J. Guibas, J. Tremblay, S. Khamis *et al.*, “Efficient geometry-aware 3d generative adversarial networks,” in *Proceedings of the IEEE/CVF conference on computer vision and pattern recognition*, 2022, pp. 16 123–16 133.
- [30] Z. Dong, X. Chen, J. Yang, M. J. Black, O. Hilliges, and A. Geiger, “Ag3d: Learning to generate 3d avatars from 2d image collections,” in *Proceedings of the IEEE/CVF international conference on computer vision*, 2023, pp. 14 916–14 927.
- [31] Z. Xu, J. Zhang, J. H. Liew, J. Feng, and M. Z. Shou, “Xagen: 3d expressive human avatars generation,” *Advances in Neural Information Processing Systems*, vol. 36, 2024.
- [32] Y. Yang, Y. Yang, H. Guo, R. Xiong, Y. Wang, and Y. Liao, “Urban-graffite: Representing urban scenes as compositional generative neural feature fields,” in *Proceedings of the IEEE/CVF International Conference on Computer Vision*, 2023, pp. 9199–9210.
- [33] B. Lei, K. Yu, M. Feng, M. Cui, and X. Xie, “Diffusiongan3d: Boosting text-guided 3d generation and domain adaptation by combining 3d gans and diffusion priors,” in *Proceedings of the IEEE/CVF Conference on Computer Vision and Pattern Recognition*, 2024, pp. 10 487–10 497.
- [34] S. An, H. Xu, Y. Shi, G. Song, U. Y. Ogras, and L. Luo, “Panohead: Geometry-aware 3d full-head synthesis in 360deg,” in *Proceedings of the IEEE/CVF conference on computer vision and pattern recognition*, 2023, pp. 20 950–20 959.
- [35] J. Sun, X. Wang, Y. Shi, L. Wang, J. Wang, and Y. Liu, “Ide-3d: Interactive disentangled editing for high-resolution 3d-aware portrait synthesis,” *ACM Transactions on Graphics (ToG)*, vol. 41, no. 6, pp. 1–10, 2022.
- [36] K. Jiang, S.-Y. Chen, F.-L. Liu, H. Fu, and L. Gao, “Nerffaceediting: Disentangled face editing in neural radiance fields,” in *SIGGRAPH Asia 2022 Conference Papers*, 2022, pp. 1–9.
- [37] Y. Deng, J. Yang, J. Xiang, and X. Tong, “Gram: Generative radiance manifolds for 3d-aware image generation,” in *Proceedings of the IEEE/CVF conference on computer vision and pattern recognition*, 2022, pp. 10 673–10 683.
- [38] F. Hong, Z. Chen, Y. Lan, L. Pan, and Z. Liu, “Eva3d: Compositional 3d human generation from 2d image collections,” *arXiv preprint arXiv:2210.04888*, 2022.
- [39] R. Abdal, W. Yifan, Z. Shi, Y. Xu, R. Po, Z. Kuang, Q. Chen, D.-Y. Yeung, and G. Wetzstein, “Gaussian shell maps for efficient 3d human generation,” in *Proceedings of the IEEE/CVF Conference on Computer Vision and Pattern Recognition*, 2024, pp. 9441–9451.
- [40] X. Chen, J. Huang, Y. Bin, L. Yu, and Y. Liao, “Veri3d: Generative vertex-based radiance fields for 3d controllable human image synthesis,” in *Proceedings of the IEEE/CVF International Conference on Computer Vision*, 2023, pp. 8986–8997.
- [41] X. Cao, H. Santo, B. Shi, F. Okura, and Y. Matsushita, “Bilateral normal integration,” in *European Conference on Computer Vision*. Springer, 2022, pp. 552–567.
- [42] Y. Choi, Y. Uh, J. Yoo, and J.-W. Ha, “Stargan v2: Diverse image synthesis for multiple domains,” in *Proceedings of the IEEE/CVF conference on computer vision and pattern recognition*, 2020, pp. 8188–8197.
- [43] Z. Liu, P. Luo, S. Qiu, X. Wang, and X. Tang, “Deepfashion: Powering robust clothes recognition and retrieval with rich annotations,” in *Proceedings of the IEEE conference on computer vision and pattern recognition*, 2016, pp. 1096–1104.
- [44] M. Heusel, H. Ramsauer, T. Unterthiner, B. Nessler, and S. Hochreiter, “Gans trained by a two time-scale update rule converge to a local nash equilibrium,” *Advances in neural information processing systems*, vol. 30, 2017.
- [45] M. Bińkowski, D. J. Sutherland, M. Arbel, and A. Gretton, “Demystifying mmd gans,” *arXiv preprint arXiv:1801.01401*, 2018.

- [46] P. Wang, L. Liu, Y. Liu, C. Theobalt, T. Komura, and W. Wang, “Neus: Learning neural implicit surfaces by volume rendering for multi-view reconstruction,” *arXiv preprint arXiv:2106.10689*, 2021.